Journal of Materials Chemistry A

PAPER

View Article Online
View Journal | View Issue

Cite this: J. Mater. Chem. A, 2015, 3, 12031

Facile preparation of a three-dimensional Fe_3O_4/macroporous graphene composite for high-performance Li storage†

Xiaoyu Lu, Ronghua Wang, Yang Bai, Jingjing Chen and Jing Sun*

Received 11th March 2015
Accepted 27th April 2015

DOI: 10.1039/c5ta01803j

www.rsc.org/MaterialsA

A three-dimensional macroscopic Fe_3O_4/porous graphene (FPG) composite was prepared by a facile self-assembly method at room temperature using polystyrene spheres as templates, followed by calcination treatment. FPG with a 3D macroporous graphene framework tightly anchored with Fe_3O_4 nanoparticles (NPs) ensures a reversible reaction and fast electron/Li^+ transport of the FPG electrode. Benefiting from the interconnected graphene framework and macropores, the FPG electrode shows a decreasing SEI and contact resistances during long-term cyclic tests with lower contact resistance and faster Li^+ diffusion compared to the contrastive Fe_3O_4/GS composed of numerous 2D hybrid sheets. As an anode material for LIBs, FPG exhibits superb rate capabilities (1057, 843, 709, 569 and 500 mA h g^{-1} at current densities of 200, 400, 800, 2000 and 4000 mA g^{-1}) and excellent long-term cyclic performance of 859 mA h g^{-1} after 1000 cycles at 2 A g^{-1} rate, which is much better than that of Fe_3O_4/GS.

1 Introduction

Rechargeable lithium-ion batteries (LIBs) have been widely used in portable devices and have gained increasing attention in the field of hybrid electric vehicles and distributed power generation applications.[1,2] To realize higher energy density and power density, metal oxides (MO) of all kinds, possessing much higher capacity than commercially used graphite, as well as eco-friendliness and natural abundance, are explored and studied as promising anode materials of LIBs.[3,4] Among these transition metal oxides, Fe_3O_4 is dominant due to its high electric conductivity and high theoretical capacity of 922 mA h g^{-1}.[5] However, Fe_3O_4 based electrodes still suffer from poor cycling performance and rate capability owing to ineffective Li^+ and electron transport along with large specific volume changes upon cycling.[6] To address these issues, diverse strategies have been proposed through special nanostructure designing, amorphous carbon coating and constructing hybrid materials with carbon nanotubes or graphene.[7–11]

Graphene, typically defined as a monolayer of sp^2 carbon atoms packed into a honey comb crystal structure, has raised great research interest as an electrode material for LIBs owing to the following features: first, large specific surface area and outstanding electrical conductivity are ideal for the storage and transport of Li^+ and electrons. Second, 2D graphene sheets with excellent mechanical properties can buffer the volume changes during Li^+ insertion/extraction.[12] These advantages make the graphene/MO composite a promising candidate for novel LIB applications. To date, the means to prepare Fe_3O_4/rGO hybrids are mainly divided into three categories: wrapping, encapsulating and anchoring.[13–18] Although enhanced specific capacity has been obtained, some drawbacks of these hybrids as electrode materials still exist. In the first two types, metal oxides still suffer from aggregation and pulverization due to their loose interaction with graphene sheets. The third type has a problem with large interface contact resistance among numerous graphene-based nanosheets.[19] To deal with these problems, researchers have designed various materials with a 3D porous electrical conductive framework, including a carbon/graphene-based and metal-based composite for LIBs to facilitate effective electron and Li-ion transport in the electrode.[20–29] In a simplified mode of lithiation reactions in LIBs, electrons transport from the current collector along conductive paths, while Li^+ diffuse through an electrolyte and bulk material. They meet at the reactive sites and the charge transfer process takes place. The electrochemical reactions are mostly determined by the electron/Li^+ transport and solid-state reaction of Li^+ and MO. The electrode materials with a 3D porous conductive framework possess (i) high electron conductivity in the continuous framework, (ii) large open pores filled with the electrolyte for fast Li^+ diffusion and buffering volume changes, (iii) short Li-ion diffusion length in the solid-state nanosized active material and (iv) large surface area with more reactive sites.[25] There are many ways to construct such a 3D porous structure, *e.g.* self-assembly of graphene by a hydrothermal method[27,28,30] and electrodeposition of conductive metals using spherical

The State Key Lab of High Performance Ceramics and Superfine Microstructure, Shanghai Institute of Ceramics, Chinese Academy of Sciences, 1295 Ding Xi Road, Shanghai 200050, China. E-mail: jingsun@mail.sic.ac.cn

† Electronic supplementary information (ESI) available. See DOI: 10.1039/c5ta01803j

templates.[25] Among these, a 3D porous graphene framework prepared by a sacrificial template is advantageous for a tunable structure and apt to hybridize with MO.[23,24,31] However, complex synthesis processes of this method such as pH control, freeze drying and additional hydrothermal treatment to incorporate with MO limited its application.[23,32] Moreover, the superior electrochemical performance of 3D macroporous graphene/MO compared to a 2D graphene/MO sheet-like composite and the mechanism behind have not yet been clearly understood.

Herein, we proposed a facile calcination synthesis of a three-dimensional Fe_3O_4 NPs/porous graphene (FPG) composite as an anode material for LIBs, using carboxylic polystyrene (c-PS) spheres as the template. Due to the strong electrostatic interaction between oppositely charged $Fe(OH)_3$/GO sheets and c-PS spheres, the self-assembly process of the two precursors was conducted at room temperature with no special treatment, followed by calcination treatment to remove the template. The as-prepared composite shows a continuous 3D macroporous graphene framework uniformly anchored with ~20 nm Fe_3O_4 NPs, exhibiting great morphological stability and electrochemical activity. Benefiting from the unique characteristics, the optimized FPG electrode displays enhanced rate capability (1057, 843, 709, 569 and 500 mA h g^{-1} at 200, 400, 800, 2000 and 4000 mA g^{-1}) and cyclic stability at high current density (859 mA h g^{-1} after 1000 cycles at 2 A g^{-1}), which is better than the Fe_3O_4/GS and most other Fe_3O_4/graphene hybrids reported.[13,33–36] Further EIS analysis reveals that the superior performance of FPG can be explained by a low contact resistance owing to the interconnected graphene framework and faster ion diffusion owing to open macropores. The structure stability of FPG that brings about excellent long-term cyclic performance is confirmed by reduced internal resistances and SEM observations of FPG after cycling.

2 Experimental

2.1 Material preparation

Preparation of c-PS spheres. c-PS spheres were synthesized using a suspension polymerization method.[37,38] In detail, 100 mL distilled water, 0.12 g $NaHCO_3$, 5 mL styrene and 0.5 mL acrylic acid were successively added into a three-necked reaction flask. After being heated at 70 °C under magnetic stirring, 0.2 g potassium persulfate as an initiator was added into the flask. The solution was kept at 70 °C for 6 h and then 90 °C for 1 h. After being washed with distilled water and centrifuged several times, c-PS was finally dispersed in water.

Preparation of $Fe(OH)_3$ sol. 0.27 g $FeCl_3 \cdot 6H_2O$ was dissolved in 10 mL distilled water to obtain a $FeCl_3$ solution. The solution was then dropwise added into 60 mL boiling distilled water and a $Fe(OH)_3$ sol was obtained.

Preparation of the FPG composite. Graphene oxide (GO) was prepared using a modified Hummers' method and dispersed in deionized water.[39,40] The $Fe(OH)_3$ sol was added into 80 mL GO solution (2 mg mL^{-1}) dropwise followed by magnetic stirring for 30 min. Next, a certain amount of c-PS solution (containing 70 mg c-PS) was dropwise added into the mixture while stirring. The resulting composite was collected after several washing and centrifugation and dried in a vacuum oven at 80 °C. Finally, the product was transferred to a tube furnace and calcined at 550 °C for 2 h under an Ar atmosphere. As a control, Fe_3O_4/GS was fabricated through the same process as FPG but without the addition of c-PS.

2.2 Material characterization

Thermogravimetry analysis was carried out with a NETZSCH STA 449C in the temperature range of 40–800 °C at a heating rate of 10 °C min^{-1} in air. Morphology of the samples was characterized with a field emission scanning microscope (Hitachi S4800) system and a transmission electron microscope (JEM-2100F at 200 kV). The Zeta potential was measured using a Zeta plus in pure water at pH = 5. X-ray diffraction (XRD) was carried out on a D/max 2550V X-ray diffraction-meter with Cu-Kα at λ = 1.5406. Raman spectra were recorded on a DXR Raman Microscope, Thermal Scientific Corporation, USA, with a 532 nm excitation length. Fourier transform infrared (FT-IR) spectra were recorded on a Thermo Scientific Nicolet iN10. X-ray photoelectron spectroscopy (XPS) analysis was conducted using a twin anode gun, Mg Kα (1253.6 eV) (Microlab 310F Scanning Auger Microprobe, VG SCIENTIFIC LTD). N_2 adsorption/desorption isotherms were determined using a Micromeritics ASAP2010 Analyzer (USA).

2.3 Electrochemical measurements

The cyclic voltammetry (CV) test was conducted on a CHI660 electrochemical workstation in a voltage range of 3.0–0 V at a scan rate of 0.5 mV s^{-1}. Nyquist plots were measured with the same workstation and all the half-cells were discharged to 0.005 V. Active materials were mixed with acetylene black and a polyvinylidene fluoride (PVDF) binder in a weight ratio of 80 : 10 : 10 to form a uniform slurry. After coating the slurry onto a copper foil, the electrode was dried in a vacuum oven at 80 °C for 20 h. The electrolyte used was 1 M $LiPF_6$ in a 50 : 50 w/w mixture of ethylene carbonate (EC) and dimethyl carbonate (DMC). The half cells with lithium flakes as counter electrodes were assembled in CR2016 type coin cells in an argon-filled glove box with the concentration of moisture and oxygen below 1 ppm. Galvanostatical discharge and charge processes were tested using a Land battery program-control test system (CT2001A) over a voltage range of 0.005–3.0 V *versus* Li/Li^+.

3 Results and discussion

The route for 3D macroscopic FPG material preparation is illustrated in Scheme 1. As we know, GO sheets in aqueous solution are usually negatively charged within a wide range of pH conditions for the abundant oxygen-containing groups on the surface and edges.[17] The exact pH range varied because of different degrees of oxidization. In our experiment, positively charged $Fe(OH)_3$ colloidal nanoparticles were first attracted onto negatively charged GO sheets (Zeta potential = −28.84 mV, Table S1†) in a pH = 5 aqueous solution, forming positively charged $Fe(OH)_3$/GO nanosheets (Zeta potential = 27.77 mV). The electrostatic repulsion between $Fe(OH)_3$ NPs and attraction

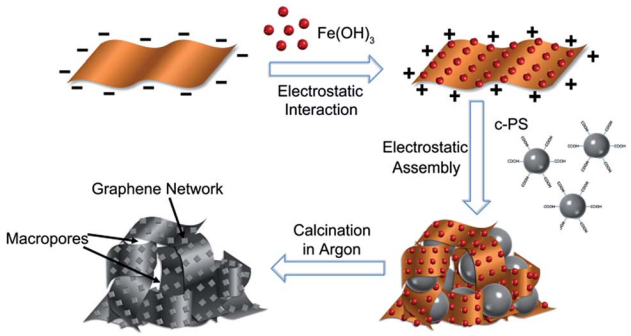

Scheme 1 Schematic illustration of the synthesis procedure for FPG.

between GO and $Fe(OH)_3$ ensured well dispersion and strong adhesion on the GO surface of $Fe(OH)_3$ NPs. Moreover, such $Fe(OH)_3$/GO hybrid sheets remained highly flexible, which can be manipulated to form a 3D porous interconnected structure with the help of a c-PS template. Acrylic acid used in styrene polymerization decorated c-PS spheres with rich carboxylic groups, which endowed c-PS spheres with a negatively charged surface (Zeta potential = −54.40 mV at pH = 5) and aqueous solubility. When added into the $Fe(OH)_3$/GO suspension, c-PS spheres with an average diameter of about 300 nm (Fig. S1†) were entrapped in pliable $Fe(OH)_3$/GO sheets, forming a $Fe(OH)_3$/GO/c-PS mixture. Unlike the core–shell structure, the $Fe(OH)_3$/GO sheets connected with each other forming a whole owing to their much larger 2D area than the diameter of c-PS.[20] It is noteworthy that all the above procedures were conducted at room temperature owing to strong electrostatic forces between oppositely charged $Fe(OH)_3$&GO and $Fe(OH)_3$/GO&c-PS. During the calcination treatment, $Fe(OH)_3$ and GO were converted to Fe_3O_4 and rGO, respectively. Meanwhile, original c-PS spheres went through pyrolysis and carbonization processes.[41,42] The released pyrolytic gaseous monomers helped creating open macropores in the FPG,[43] inducing the three-dimensional porous graphene framework anchored with nanosized Fe_3O_4 particles.

As mentioned above, the unique structure of $Fe(OH)_3$/GO/c-PS induced the formation of 3D macroporous FPG. The SEM image (Fig. 1a) shows that c-PS spheres on the surface are covered with $Fe(OH)_3$/GO sheets. Closely packed c-PS spheres with $Fe(OH)_3$/GO sheets on them are observed (Fig. 1b), for which we speculate that the majority of c-PS and $Fe(OH)_3$/GO are arranged in a similar way. Further TEM observations are conducted after drastic ultrasonication and grinding, which were used to disperse the material. As shown in Fig. 1c, the c-PS spheres are still closely attached to $Fe(OH)_3$/GO sheets, which suggests the structural stability of $Fe(OH)_3$/GO/c-PS prepared only by adding the three agents in an appropriate order. The 3–5 nm polycrystalline $Fe(OH)_3$ particles show good dispersibility on ~5 layered GO sheets (Fig. 1d), which determines well-dispersed Fe_3O_4 NPs that further inhibits agglomeration and pulverization of the active material during Li^+ insertion/extraction processes'.

After the calcination treatment, FPG with a continuous Fe_3O_4/GS framework retains its original construction instead of collapsing after c-PS spheres vanish. SEM and TEM images (Fig. 2) of the as-prepared FPG composite exhibit a well-defined 3D hierarchical macroporous architecture. SEM images (Fig. 2a and b) show that the whole FPG composite surface is covered with numerous orderly arranged pores of about 300 nm in diameter. Closer observations (Fig. 2c) reveal a continuous thin-walled graphene framework with evenly dispersed Fe_3O_4 NPs, which would facilitate efficient electron transport to the active material. As shown in the TEM image (Fig. 2d), the FPG owns a well-defined hierarchical structure with close-packed spherical macropores. Induced by the gaseous monomers released from the embedded c-PS spheres, these macropores are interconnected to each other and form a 3D open structure. On the graphene framework, 10–30 nm Fe_3O_4 NPs are evenly dispersed (Fig. 2e), showing crystal growth from original $Fe(OH)_3$ (~5 nm). The interplanar spacing of Fe_3O_4 NPs is 0.25 nm and 0.29 nm (Fig. 2f), corresponding to the (311) and (220) facet of magnetite Fe_3O_4, which is consistent with the SAED pattern (inset of Fig. 2f). In comparison, the Fe_3O_4/GS composite with the same thermal treatment exhibits a completely different structure, in which numerous crumpled Fe_3O_4/GS sheets are randomly assembled (Fig. S2†). When the FPG composite is used as an electrode for LIBs, the large porosity and intense adhesion of Fe_3O_4 NPs on the graphene framework would restrict the expansion and contraction of Fe_3O_4 NPs during cycling, which leads to enhanced cyclic performance. The small size of Fe_3O_4 facilitates fast Li^+ diffusion in bulk materials. Moreover, the 3D conductive graphene framework with interconnected open pores could shorten both electric and Li^+ diffusion distances, which results in improved rate capability.

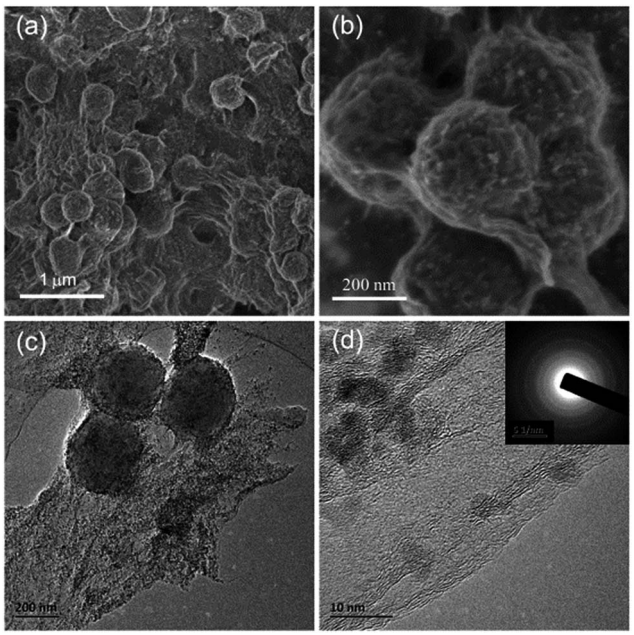

Fig. 1 (a and b) SEM images of the $Fe(OH)_3$/GO/c-PS at different magnifications; (c) TEM image of the $Fe(OH)_3$/GO/c-PS, (d) HRTEM image of the $Fe(OH)_3$/GO/c-PS at the fringe region, (inset of d) the corresponding SEAD pattern reveals polycrystalline $Fe(OH)_3$.

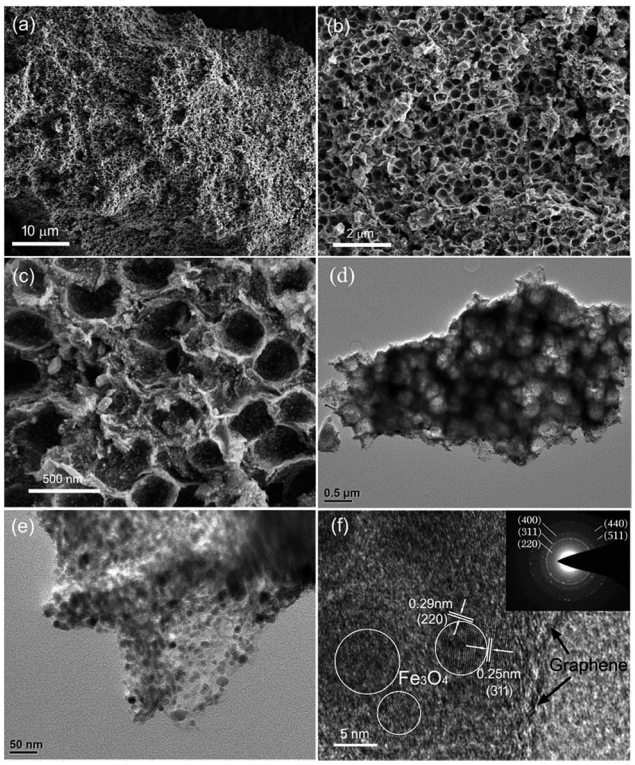

Fig. 2 (a–c) SEM images of the FPG at different magnifications; (d and e) TEM images of the FPG at different magnifications; (f) HRTEM image of the FPG, the inset is the corresponding SAED pattern.

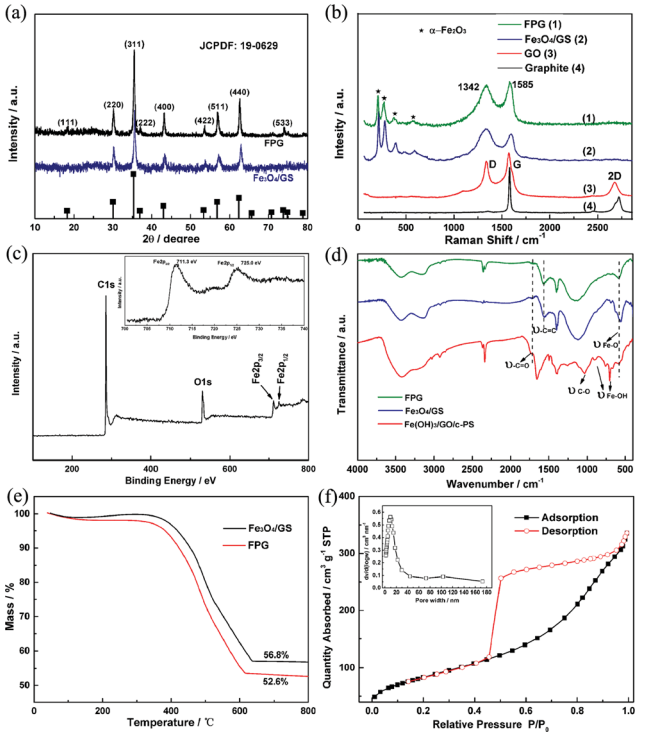

Fig. 3 Sample characterization: (a) XRD patterns of FPG and Fe_3O_4/GS; (b) TG curves of FPG and Fe_3O_4/GS; (c) XPS spectrum of the FPG; (inset of c) Fe 2p core-level XPS spectrum; (d) FT-IR spectra of the FPG, Fe_3O_4/GS and $Fe(OH)_3$/GO/c-PS; (e) Raman spectra of FPG, Fe_3O_4/GS, GO and pristine graphite; (f) nitrogen adsorption–desorption isotherms and (inset of f) pore size distribution of FPG.

XRD patterns of the FPG and Fe_3O_4/GS are shown in Fig. 3a, the peaks of both composites can well be indexed to magnetite Fe_3O_4 (JCPDS no. 19-0629), or cubic γ-Fe_2O_3 (JCPDS no. 39-1346). The average size of Fe_3O_4 NPs in the FPG is calculated to be 24 nm by half peak width according to the Scherrer equation, which is consistent with the TEM observation. Raman spectra of the FPG and Fe_3O_4/GS (Fig. 3b) indicate the existence of α-Fe_2O_3 (A_{1g}: 212 nm^{-1}; E_g: 277, 377 and 573 nm^{-1}). This can be attributed to the decomposition of Fe_3O_4 to α-Fe_2O_3 simulated by laser light (532 nm) used in Raman measurements.[11,44,45] The graphene hybrids show a typical D band and G band at around 1344 and 1586 nm^{-1}. The larger I_D/I_G ratio of FPG (0.92) than that of GO (0.81) indicates diminishing of sp^2 hybridized carbon.[46,47] Besides, the lower I_D/I_G ratio of FPG than that of Fe_3O_4/GS (1.20) is probably caused by the pyrolyzed residue of c-PS.[48,49] To prove this, we further performed Raman spectroscopy for calcined c-PS prepared with the same heat treatment as FPG (Fig. S3†). The pyrolyzed residue of c-PS shows strong peaks and a very low I_D/I_G ratio of 0.84 (Table S2†) due to the numerous aromatic monomers in c-PS.[7] Fig. 3c shows a wide scan XPS spectrum of FPG, which confirms the presence of C 1s, O 1s and Fe 2p. The core-level C 1s spectrum of FPG consists of three main components, accounting for C–C/C=C (285.0 eV), C–O (286.5 eV), C=O (287.6 eV). FPG is well reduced according to the large C/O ratio.[28] The peaks located at 711.3 eV and 725.0 eV are attributed to Fe $2p_{3/2}$ and Fe $2p_{1/2}$, respectively, and there are no obvious satellites for γ-Fe_2O_3.[50–52] Fourier transform infrared (FT-IR) spectra of FPG, Fe_3O_4/GS and $Fe(OH)_3$/GO/c-PS are shown in Fig. 3d. Instead of typical multipeaks of γ-Fe_2O_3, only one peak of FPG at 585 cm^{-1} is found and assigned to Fe–O stretching vibration modes in stoichiometric Fe_3O_4.[28,33,36,50] The peaks of $Fe(OH)_3$/GO/c-PS at 702, 755 and 898 cm^{-1} are possibly attributed to bending vibrations of Fe–OH.[28] Those ones disappear in the spectrum of FPG due to the transformation from $Fe(OH)_3$ to Fe_3O_4. The absorption bands of carboxyl C=O at 1720 cm^{-1} and epoxy C–O at 1030 cm^{-1} obviously decrease after calcination, showing effective reduction of graphene in FPG.[33,53] Thermogravimetry analysis (TGA) was conducted to determine the Fe_3O_4 content in FPG and Fe_3O_4/GS. The weight loss before 200 °C is attributed to water gasification. After heating to 800 °C, the FPG is completely converted to Fe_2O_3, with an overall weight loss of 47.4 wt%. According to this, Fe_3O_4 contents in the FPG and Fe_3O_4/GS hybrids are calculated to be 51.8 wt% and 55.3 wt%, respectively (Fig. 3e). The nitrogen adsorption–desorption isotherms of the FPG shown in Fig. 3f is type IV, with a H2 hysteresis loop at a relative pressure of 0.5–1 (P/P_0). The BET surface area of this FPG is 301.7 $m^2\ g^{-1}$, while Fe_3O_4/GS shows a slightly larger value of 371.9 $m^2\ g^{-1}$ (Fig. S5†). On one hand, the typical ~300 nm macropores in FPG contribute little to the total BET surface (inset of Fig. 3f).[54] On the other hand, the c-PS residue could reduce the BET by taking up some weight proportion. In a word, FPG is similar to Fe_3O_4/GS in most characters except for the unique 3D hierarchical porous structure by rational design.

All the electrochemical tests of the FPG and Fe_3O_4/GS are carried out in a coin cell. To evaluate the cyclic performance of the FGP, we performed the cyclic voltammetry test at 0.5 mV s^{-1} scan rate in 0–3.0 V voltage range. As shown in Fig. 4a, the FPG exhibits a shoulder peak at about 1.3 V in the first cycle, corresponding to diffusion of Li^+ into Fe_3O_4 crystal lattice forming $Li_xFe_3O_4$,[8,55] but it disappears in the following cycles. A broad peak at ~0.25 V reveals a reduction reaction from Fe^{3+} and Fe^{2+} to Fe^0, as well as Li-ion insertion into graphene layers and surface. Then the only reduction peak shifts to a higher voltage with a lower current response and narrower peak. On the other hand, broad oxidation peaks at ~1.65 V, which could be attributed to the oxidation reaction from Fe^0 to Fe^{2+} and Fe^{3+}, are found in the 1st and subsequent anodic processes. It is noteworthy that from the 2nd sweep cycle, the CV peaks of different cycles move to ~1.75 V and overlap on one another, which indicates a good reversibility of the discharge–charge reaction of the composite.

Long-term cyclic performance and the rate capability of the FPG and Fe_3O_4/GS electrodes are performed with galvanostatic discharge–charge measurements at various current densities from 100 to 4000 mA g^{-1}. The discharge and charge curves of FPG shown in Fig. 4b reveal a reversible capacity of 1154 mA h g^{-1} at 100 mA g^{-1} after 180 cycles. The 1st discharge and charge capacities are 1480.9 and 1139.1 mA h g^{-1}. The low Coulombic efficiency of 76.9% is mainly due to the solid electrolyte interface (SEI) formation and other irreversible electrochemical reactions.[9] It increases rapidly to 93.9% in the 2nd cycle and retains above 98.5% after 25 cycles (Fig. S6†). The specific capacity of FPG slightly decreases in the first 50 cycles, then increases gradually in the following cycles. Taking the CV results into consideration, the conversion reaction of ferric oxide mostly takes place above 0.7 V. As a result, we separate the overall discharge capacity into two parts: the capacity owing to then Fe_3O_4 conversion reaction and other Li^+ storage mostly contributed by the graphene framework (inset of Fig. 4b).[49] The first part of capacity declines from 563.2 mA h g^{-1} (5th), 523.4 mA h g^{-1} (20th) to 441.5 mA h g^{-1} (50th) and thereafter remains stable until the 180th cycle (442.1 mA h g^{-1}), which implies that the Fe_3O_4 NPs undergo limited pulverization and agglomeration in the first few cycles. Invertible reactions are acquired afterwards thanks to nanosized Fe_3O_4 and the confinement effect of graphene in FGP. Capacities between 0.7 and 0.005 V display an increasing tendency from 518.5 mA h g^{-1} (5th), 523.2 (20th), 582.6 mA h g^{-1} (50th) to 712.4 mA h g^{-1} (180th). Such enhancement is attributed to the large specific surface area for surface storage and structural stability of FPG, which endow stable SEI formation. As a result, capacity loss occurs in the first few cycles, while enhanced surface Li^+ storage takes the dominant position in the subsequent cycles. Compared to the Fe_3O_4/GS electrode (Fig. 4c), FPG shows better performance under different galvanostatic conditions. At a current density of 200 mA g^{-1}, the FPG and Fe_3O_4/GS electrodes exhibit capacities of 1057 and 603.3 mA h g^{-1}, respectively. When current densities are changed to 400, 800, 2000, 4000 and 200 mA g^{-1}, the FPG shows a capacity retention of 79.8%, 67.1%, 53.9%, 47.2% and 100%. However, the Fe_3O_4/GS electrode has only 75.5%, 53.7%, 31.1%, 18.8% and 84.4% of capacity retention. In a long-term cyclic performance test at a current density as high as 2 A g^{-1}, the FPG electrode shows a reversible discharge capacity of 859 mA h g^{-1} even after 1000 cycles, compared to only 201 mA h g^{-1} for Fe_3O_4/GS. To better evaluate the performance of FPG, the important and recent studies on the Fe_3O_4/graphene electrode are listed in Table S3† for comparison. The specific capacity of FPG at a low rate (0.1 A g^{-1}) is comparable to other studies. We suppose that the relatively low Fe_3O_4 weight ratio (52.6 wt%) in FPG makes it not so outstanding at a low rate. However, the performance of FPG at high rates is specially superior to Fe_3O_4/graphene with 2D sheet-like construction at present (references are listed in the ESI†). The advantages owing to the 3D interconnected graphene framework of FPG are evident, especially at high current densities. In the control Fe_3O_4/GS electrode, numerous sheets are randomly assembled, causing much longer diffusion paths for electron/Li^+ and a severe polarization effect during the fast charge/discharge process.[19] In addition, the FPG with large porosity is more capable of buffering the volume changes during cycling, which greatly enhances the cyclability.

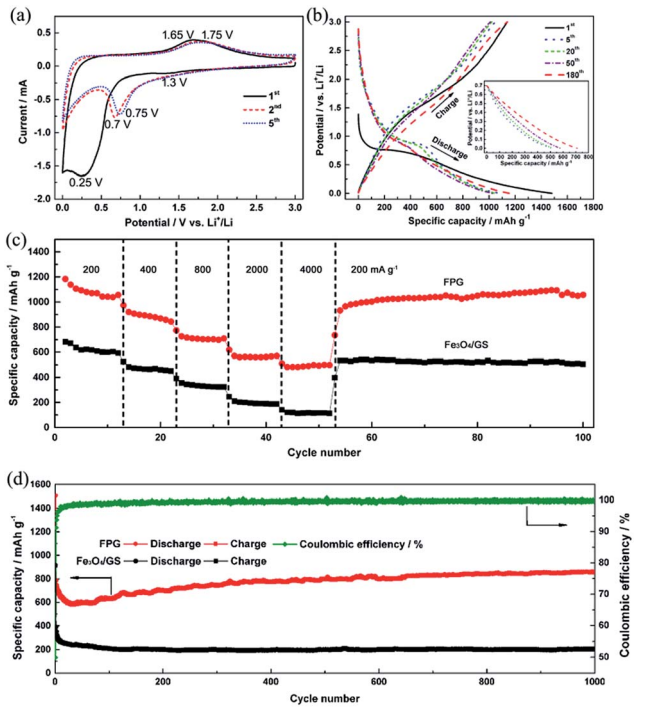

Fig. 4 (a) Cyclic voltammograms for the 1st, 2nd and 5th cycles of the FPG electrode; (b) charge–discharge voltage profiles of the FPG electrode at a current density of 100 mA g^{-1}, the inset is discharge voltage profiles of FPG between 0.7 V and 0.005 V; (c) rate capabilities of FPG and Fe_3O_4/GS electrodes at different current densities; (d) long-term cyclic performance of FPG and Fe_3O_4/GS electrodes at a current density of 2 A g^{-1}.

To verify the excellent performance of the FPG electrodes, we performed electrochemical impedance spectroscopy (EIS) in comparison with Fe_3O_4/GS. The Nyquist plots of both samples are shown in Fig. 5a with a frequency range of 100 kHz to 0.001 Hz. The solid electrolyte interface resistance (R_{SEI}) and the

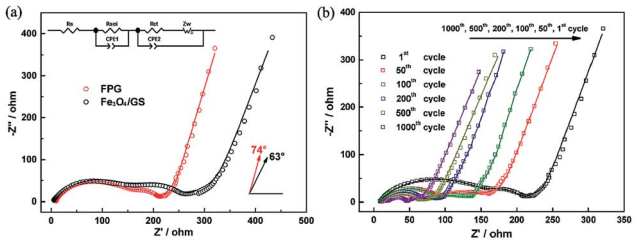

Fig. 5 Nyquist plots of (a) FPG and Fe_3O_4/GS electrodes after first discharge and (b) FPG electrode after various number of cycles at a current density of 2 A g^{-1}. Solid lines in both figures are fitted results using an equivalent circuit model in the inset of (a).

charge transfer resistance (R_{ct}) are simulated with an equivalent circuit model (inset of Fig. 5a) and the results are displayed in Fig. S7.† Similar plots at high frequency suggest comparable R_{SEI} conditions for both samples. Compared to Fe_3O_4/GS, the diameters of the semi-circles for the FPG electrode at medium frequency is much smaller, which indicates a decreased contact and charge transfer resistance.[30,56] In the low frequency region, the FPG electrode exhibits a shortened and more inclined line with a slope of 72° (63° for Fe_3O_4/GS), indicating faster Li^+ diffusion in the FPG.[57] In addition, the Nyquist plots of FPG show a trend of depressed semicircles at high/medium frequency and a shortened tail at low frequency during cycling (Fig. 5b). R_{SEI} and R_{ct} are 154 Ω and 39 Ω at the first cycle, decreasing gradually to 25 Ω and 2 Ω at the 1000th cycle, respectively. These results suggest that the FPG with a 3D structure retains well its morphology during high rate cycles. Moreover, a stabilized and partially reversible SEI film forms after a few cycles, which contributes to the enhancement of specific capacity during long-term cycling.[58–60]

SEM images of the FPG electrode after 1000 cycles at 2 A g^{-1} are shown in Fig. 6. The shape of the 3D porous structure remains well, with some surface maybe covered with aggregated ferric oxides or the SEI film. Although the original macropores are no longer found, numerous smaller pores appear instead, which are caused by extension and contraction effects as we suppose. The excellent structural stability of the interconnected 3D macroporous FPG guarantees stable SEI film formation and fast electron/Li-ion transformation even at high rates for long-term cycling.

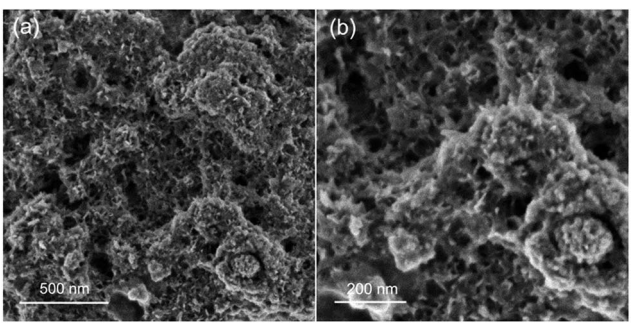

Fig. 6 SEM images of the FPG after 1000 cycles at 2 A g^{-1} current density and charged to 3.0 V.

4 Conclusion

In summary, we have developed a facile calcination method to rationally design a 3D Fe_3O_4/porous graphene composite as a high performance anode material for LIBs. Well crystallized Fe_3O_4 NPs of ~20 nm in size are homogeneously anchored on a 3D graphene framework with ~300 nm open macropores. This macroporous structure is established through strong interactions between oppositely charged $Fe(OH)_3$/GO sheets and c-PS spheres under moderate conditions. In applications of lithium-ion battery electrodes, the porous feature of FPG can help buffering the volume changes of Fe_3O_4 and greatly enhancing the electrolyte/material interfacial reactivity. As a result, such 3D macroporous FPG shows superior rate capacity and long-term cyclic performance compared to the Fe_3O_4/GS. The good structural integrity of FPG after long-term cycles at a high rate proves its ability to buffer volume changes and endow fast electron/ion transport. The lower electrode contact resistance of FPG than that of Fe_3O_4/GS with faster Li^+ diffusion is further confirmed by EIS analysis, which theoretically explains why FPG has much better performance. Our work emphasizes the advantages of rationally designing a metal oxide/carbon composite with a porous structure. The simplicity of this method makes it promising for combining precise control of hierarchical morphology from macro to micro and mass production.

Acknowledgements

This work is supported by the 973 Project (2012CB932303), the National Natural Science Foundation of China (Grant no. 50972153, 51072215 and 51172261).

Notes and references

1 J. B. Goodenough and Y. Kim, *Chem. Mater.*, 2010, **22**, 587–603.
2 A. S. Arico, P. Bruce, B. Scrosati, J. M. Tarascon and W. van Schalkwijk, *Nat. Mater.*, 2005, **4**, 366–377.
3 M. V. Reddy, G. V. Subba Rao and B. V. Chowdari, *Chem. Rev.*, 2013, **113**, 5364–5457.
4 P. Poizot, S. Laruelle, S. Grugeon, L. Dupont and J. M. Tarascon, *Nature*, 2000, **407**, 496–499.
5 Y. H. Chang, J. Li, B. Wang, H. Luo, H. Y. He, Q. Song and L. J. Zhi, *J. Mater. Chem. A*, 2013, **1**, 14658–14665.
6 L. Zhang, H. B. Wu and X. W. D. Lou, *Adv. Energy Mater.*, 2014, **4**, 1300958.
7 Y. Su, S. Li, D. Wu, F. Zhang, H. Liang, P. Gao, C. Cheng and X. Feng, *ACS Nano*, 2012, **6**, 8349–8356.
8 P. Lian, X. Zhu, H. Xiang, Z. Li, W. Yang and H. Wang, *Electrochim. Acta*, 2010, **56**, 834–840.
9 S. M. Yuan, J. X. Li, L. T. Yang, L. W. Su, L. Liu and Z. Zhou, *ACS Appl. Mater. Interfaces*, 2011, **3**, 705–709.
10 W.-M. Zhang, X.-L. Wu, J.-S. Hu, Y.-G. Guo and L.-J. Wan, *Adv. Funct. Mater.*, 2008, **18**, 3941–3946.
11 J. Z. Liu, J. F. Ni, Y. Zhao, H. B. Wang and L. J. Gao, *J. Mater. Chem. A*, 2013, **1**, 12879–12884.

12 S. Han, D. Wu, S. Li, F. Zhang and X. Feng, *Small*, 2013, **9**, 1173–1187.
13 Z.-S. Wu, G. Zhou, L.-C. Yin, W. Ren, F. Li and H.-M. Cheng, *Nano Energy*, 2012, **1**, 107–131.
14 J. Su, M. Cao, L. Ren and C. Hu, *J. Phys. Chem. C*, 2011, **115**, 14469–14477.
15 R. H. Wang, C. H. Xu, J. Sun, L. Gao and C. C. Lin, *J. Mater. Chem. A*, 2013, **1**, 1794–1800.
16 D. Chen, G. Ji, Y. Ma, J. Y. Lee and J. Lu, *ACS Appl. Mater. Interfaces*, 2011, **3**, 3078–3083.
17 M. Du, C. Xu, J. Sun and L. Gao, *J. Mater. Chem. A*, 2013, **1**, 7154–7158.
18 S. K. Behera, *Chem. Commun.*, 2011, **47**, 10371–10373.
19 Y. Gong, S. Yang, Z. Liu, L. Ma, R. Vajtai and P. M. Ajayan, *Adv. Mater.*, 2013, **25**, 3979–3984.
20 P. Wu, H. Wang, Y. Tang, Y. Zhou and T. Lu, *ACS Appl. Mater. Interfaces*, 2014, **6**, 3546–3552.
21 Q. Zhu, P. Wu, J. Zhang, W. Zhang, Y. Zhou, Y. Tang and T. Lu, *ChemSusChem*, 2015, **8**, 131–137.
22 J. Li, P. Wu, Y. Tang, X. Xu, Y. Zhou, Y. Chen and T. Lu, *CrystEngComm*, 2013, **15**, 10340–10345.
23 X. Liu, J. Cheng, W. Li, X. Zhong, Z. Yang, L. Gu and Y. Yu, *Nanoscale*, 2014, **6**, 7817–7822.
24 B. G. Choi, M. Yang, W. H. Hong, J. W. Choi and Y. S. Huh, *ACS Nano*, 2012, **6**, 4020–4028.
25 H. Zhang, X. Yu and P. V. Braun, *Nat. Nanotechnol.*, 2011, **6**, 277–281.
26 S. Nardecchia, D. Carriazo, M. L. Ferrer, M. C. Gutierrez and F. del Monte, *Chem. Soc. Rev.*, 2013, **42**, 794–830.
27 Y. Gong, S. Yang, L. Zhan, L. Ma, R. Vajtai and P. M. Ajayan, *Adv. Funct. Mater.*, 2014, **24**, 125–130.
28 H. P. Cong, X. C. Ren, P. Wang and S. H. Yu, *ACS Nano*, 2012, **6**, 2693–2703.
29 H. Yin, S. Zhao, J. Wan, H. Tang, L. Chang, L. He, H. Zhao, Y. Gao and Z. Tang, *Adv. Mater.*, 2013, **25**, 6270–6276.
30 W. Wei, S. Yang, H. Zhou, I. Lieberwirth, X. Feng and K. Mullen, *Adv. Mater.*, 2013, **25**, 2909–2914.
31 D. Fan, Y. Liu, J. He, Y. Zhou and Y. Yang, *J. Mater. Chem.*, 2012, **22**, 1396–1402.
32 D. Ma, S. Yuan and Z. Cao, *Chin. Sci. Bull.*, 2014, **59**, 2017–2023.
33 B. Li, H. Cao, J. Shao and M. Qu, *Chem. Commun.*, 2011, **47**, 10374–10376.
34 G. Zhou, D.-W. Wang, F. Li, L. Zhang, N. Li, Z.-S. Wu, L. Wen, G. Q. Lu and H.-M. Cheng, *Chem. Mater.*, 2010, **22**, 5306–5313.
35 L. Ji, Z. Tan, T. R. Kuykendall, S. Aloni, S. Xun, E. Lin, V. Battaglia and Y. Zhang, *Phys. Chem. Chem. Phys.*, 2011, **13**, 7170–7177.
36 G. Wang, T. Liu, X. Xie, Z. Ren, J. Bai and H. Wang, *Mater. Chem. Phys.*, 2011, **128**, 336–340.
37 X. Huang, H. Yu, J. Chen, Z. Lu, R. Yazami and H. H. Hng, *Adv. Mater.*, 2014, **26**, 1296–1303.
38 Z. Y. Lu, Y. Q. Qin, J. Y. Fang, J. Sun, J. Li, F. Q. Liu and A. S. Yang, *Nanotechnology*, 2008, **19**, 055602.
39 W. S. Hummers and R. E. Offeman, *J. Am. Chem. Soc.*, 1958, **80**, 1339.
40 C. H. Xu, J. Sun and L. Gao, *J. Mater. Chem.*, 2012, **22**, 975–979.
41 R. W. J. Westerhout, J. Waanders, J. A. M. Kuipers and W. P. M. van Swaaij, *Ind. Eng. Chem. Res.*, 1997, **36**, 1955–1964.
42 W. W. Lukens and G. D. Stucky, *Chem. Mater.*, 2002, **14**, 1665–1670.
43 H. Wang, D. Zhang, T. Yan, X. Wen, J. Zhang, L. Shi and Q. Zhong, *J. Mater. Chem. A*, 2013, **1**, 11778.
44 M. Sathish, T. Tomai and I. Honma, *J. Power Sources*, 2012, **217**, 85–91.
45 I. Chourpa, L. Douziech-Eyrolles, L. Ngaboni-Okassa, J. F. Fouquenet, S. Cohen-Jonathan, M. Souce, H. Marchais and P. Dubois, *Analyst*, 2005, **130**, 1395–1403.
46 A. C. Ferrari, J. C. Meyer, V. Scardaci, C. Casiraghi, M. Lazzeri, F. Mauri, S. Piscanec, D. Jiang, K. S. Novoselov, S. Roth and A. K. Geim, *Phys. Rev. Lett.*, 2006, **97**, 187401.
47 L. M. Malard, M. A. Pimenta, G. Dresselhaus and M. S. Dresselhaus, *Phys. Rep.*, 2009, **473**, 51–87.
48 W. Gao, Y. Wan, Y. Dou and D. Zhao, *Adv. Energy Mater.*, 2011, **1**, 115–123.
49 J. Zhu, D. Yang, X. Rui, D. Sim, H. Yu, H. H. Hng, H. E. Hoster, P. M. Ajayan and Q. Yan, *Small*, 2013, **9**, 3390–3397.
50 P. Wu, N. Du, H. Zhang, J. Yu and D. Yang, *J. Phys. Chem. C*, 2011, **115**, 3612–3620.
51 L. Fan, B. Li, D. W. Rooney, N. Zhang and K. Sun, *Chem. Commun.*, 2015, **51**, 1597–1600.
52 S. H. Choi and Y. C. Kang, *Carbon*, 2014, **79**, 58–66.
53 M. Zong, Y. Huang, Y. Zhao, X. Sun, C. Qu, D. Luo and J. Zheng, *RSC Adv.*, 2013, **3**, 23638–23648.
54 J. C. Groen, L. A. A. Peffer and J. Pérez-Ramírez, *Microporous Mesoporous Mater.*, 2003, **60**, 1–17.
55 L. Wang, Y. Yu, P. C. Chen, D. W. Zhang and C. H. Chen, *J. Power Sources*, 2008, **183**, 717–723.
56 Z. S. Wu, S. Yang, Y. Sun, K. Parvez, X. Feng and K. Mullen, *J. Am. Chem. Soc.*, 2012, **134**, 9082–9085.
57 K. H. Park, D. Lee, J. Kim, J. Song, Y. M. Lee, H. T. Kim and J. K. Park, *Nano Letters*, 2014, **14**, 4306–4313.
58 S. J. Prabakar, Y. H. Hwang, E. G. Bae, S. Shim, D. Kim, M. S. Lah, K. S. Sohn and M. Pyo, *Adv. Mater.*, 2013, **25**, 3307–3312.
59 R. Wang, C. Xu, J. Sun, L. Gao and H. Yao, *ACS Appl. Mater. Interfaces*, 2014, **6**, 3427–3436.
60 R. Wang, C. Xu, M. Du, J. Sun, L. Gao, P. Zhang, H. Yao and C. Lin, *Small*, 2014, **10**, 2260–2269.